## PAPER

Check for updates

# Cu–Ag interactions in bimetallic Cu–Ag catalysts enhance C$_{2+}$ product formation during electrochemical CO reduction†

Floriane A. Rollier,[a] Valery Muravev,[a] Nikolay Kosinov, [ID][a] Tim Wissink,[a] Dimitra Anastasiadou,[a] Bianca Ligt,[a] Laurent Barthe,[b] Marta Costa Figueiredo [ID][a] and Emiel J. M. Hensen [ID] *[a]

The electroreduction of CO (CORR) is a promising alternative to the direct CO$_2$ electroreduction reaction (CO2RR) to produce C$_{2+}$ products. Cu-based electrocatalysts enable the formation of C–C bonds, leading to various C$_{2+}$ hydrocarbon and oxygenate products. Herein, we investigated how the composition of bimetallic Cu–Ag catalysts impacted the nature of the Cu–Ag interactions and the product distribution of the CORR, aiming to improve the selectivity to C$_{2+}$ products. Cu–Ag catalysts containing 1–50 mol% Ag were prepared by sol–gel synthesis. A Ag content of 10 mol% of Ag (Cu$_{0.9}$Ag$_{0.1}$) was optimum with respect to increasing the C$_{2+}$ product selectivity and suppressing H$_2$ evolution. *Operando* X-ray absorption spectroscopy and quasi-*in situ* X-ray photoelectron spectroscopy demonstrated the complete reduction of CuO to Cu during CORR. Electron microscopy (EM) and *in situ* wide-angle X-ray scattering (WAXS) revealed substantial restructuring during reduction. EM imaging showed the formation of Ag–Cu core–shell structures in Cu$_{0.9}$Ag$_{0.1}$, while separate Cu and Ag particles were predominant at higher Ag content. *In situ* WAXS revealed the formation of a Cu–Ag nanoalloy phase in the bimetallic Cu–Ag samples. The optimum Cu$_{0.9}$Ag$_{0.1}$ sample contained more Cu–Ag nanoalloys than samples with a higher Ag content. The Cu–Ag interfaces between the Ag-core and the Cu-shell in the bimetallic particles are thought to host the nanoalloys. The optimum CORR performance for Cu$_{0.9}$Ag$_{0.1}$ is likely due to the enhanced Cu–Ag interactions, as confirmed by a sample prepared with the same surface composition by galvanic exchange.

## 1 Introduction

The electrochemical reduction reaction of carbon monoxide (CORR) to products containing C–C bonds (C$_{2+}$ products) has seen increasing scientific interest in recent years.[1–6] Mechanistic investigations of the related CO$_2$ electroreduction reaction (CO2RR) showed the pivotal role of CO as the critical surface intermediate in the formation of C–C bonds in C$_{2+}$ products.[7–10] Consequently, replacing CO$_2$ with CO as the carbon source may enhance the selectivity to C$_{2+}$ compounds. Previous reports confirmed this by showing a higher selectivity for products like ethylene, ethanol, and acetate using CO instead of CO$_2$.[3,11,12] In a two-step strategy, the reduction of CO$_2$ to CO, involving a two-electron transfer, would first be carried out, followed by the

conversion of CO to C$_{2+}$ products. While for CO2RR, a C=O dissociation step is necessary to proceed to C–C coupling, this is not the case for CORR. Moreover, forming a mole of product from CO requires fewer electrons than CO2RR. These two factors may favor the formation of C$_{2+}$ products in CORR, as reported in some recent studies.[6,13]

Catalyst design approaches are increasingly employed to improve the selectivity of thermal and electrochemical catalytic processes.[14–19] In his early work, Hori screened many metals for CO2RR and CORR in search of a suitable metal-selectivity descriptor.[20] Among the investigated metals, only Cu-based catalysts could convert CO$_2$ and CO to C$_{2+}$ products.[10,20,21] The typical product distribution on Cu includes, among other products, ethylene, propylene, ethanol, propanol, and acetic acid. Yet, the similar mechanistic pathways shared among these products result in poor selectivity of the CORR[10,22,23] and impede the further development of the technology towards practical applications.[24]

Control over the morphology and composition of electrocatalysts is often employed to tune their performance towards CO2RR and CORR.[14,25–27] Adding another metal to Cu alters the product distribution by modifying the surface sites and the

*[a] Laboratory of Inorganic Materials and Catalysis, Department of Chemical Engineering and Chemistry, Eindhoven University of Technology, P.O. Box 513, 5600 MB Eindhoven, The Netherlands. E-mail: e.j.m.hensen@tue.nl*

*[b] Synchrotron SOLEIL, L'Orme des Merisiers, Départementale 128, 91190 Saint-Aubin, France*

binding properties of reaction intermediates. Metals selective to CO formation, such as Au, Ag, and Zn, have been used as co-catalysts in CO2RR to enable sequential electroreduction of $CO_2$ to CO, followed by the conversion of CO to target products.[27–31] In a tandem fashion, CO is primarily produced on the co-catalyst, and the spillover of CO to Cu results in high reactant coverage. The abundance of CO intermediate in the double layer facilitates C–C coupling reactions, enhancing the selectivity to $C_{2+}$ products.[27–31] Moreover, interactions between Cu and CO-selective metals were beneficial, as interfacial sites and the formation of alloys improve the selectivity to $C_{2+}$ products in CO2RR.[30,32–36] For instance, Huang *et al.* developed Cu–Ag nanodimers possessing tandem and interfacial catalysis sites. At the interfacial sites, the formation of a Cu–Ag nano-alloy, hosting electronic effects between Cu and Ag, was beneficial for the formation of $C_{2+}$ products.[37]

Earlier works on CORR focused exclusively on bimetallic catalysts prepared by galvanic exchange.[19,38,39] This method implies the spontaneous replacement of surface Cu by Ag upon immersion of Cu metal in a solution containing $Ag^+$ ions.[38,39] Some reports mentioned that the presence of Ag in a surface alloy maintains part of the Cu atoms in a $Cu^{\delta+}$ state.[33,40] CO molecules bind more strongly on these sites, which increases the CO residence time on the surface and, therefore, the probability of C–C coupling reactions. Conversely, other reports emphasized the fully reduced state of Cu–Ag catalysts, which was observed almost immediately after applying a negative potential.[19,38,39] Some of these works correlated the better performance to strain and ligand effects, which reduce the activation energy of $C_1$ to $C_1$ and $C_1$ to $C_2$ coupling, widen the d-band, and promote electron transfer from Cu to Ag.[19,38,39] As the nature of Cu–Ag interfacial sites under CORR conditions remains elusive, *in situ* characterization is required to confirm their presence. Moreover, the role of bimetallic Cu–Ag electro-catalysts for CORR has only been scarcely investigated.[19,38,39] As a result, the nature of the active phase, its oxidation state, and possible restructuring under reaction conditions are valuable topics of investigation.

In this study, we synthesized bimetallic Cu–Ag catalysts using a one-pot sol–gel method to increase the interactions between the two metals. The Cu–Ag composition substantially impacted the selectivity to $C_{2+}$ products during CORR. In particular, the $C_{2+}$ product selectivity was the highest (faradaic efficiency 63%) for the sample containing 10 mol% Ag. While *ex situ* characterization by XPS clearly demonstrated differences in Cu–Ag interactions in the as-prepared samples of different composition, *operando* XAS and *in situ* WAXS highlighted the structural differences between the reduced samples during the CORR. The addition of 10 mol% Ag in $Cu_{0.9}Ag_{0.1}$ caused the expansion of the Cu lattice due to the formation of nanoalloys. STEM-EDX imaging of used samples showed the formation of Ag–Cu core–shell structures at low Ag content, while mostly separated Cu and Ag particles were observed at high Ag content (50 mol% Ag). The extent of Cu–Ag interactions explained the catalytic performance differences as a function of the Ag content.

# 2 Results and discussion

## 2.1. CORR performance

Several Cu–Ag bimetallic catalysts of different compositions (Ag content 1–50 mol%) and monometallic references (Cu-only and Ag-only) were prepared using a one-pot sol–gel synthesis method (Fig. 1a). The composition of the obtained samples was confirmed by elemental analysis (inductively coupled plasma-optical emission spectrometry (ICP-OES)) (Table S2†). The performance of these samples was tested in CORR under strongly alkaline conditions (3 M KOH). At a mild potential of −0.4 V *vs.* RHE (Fig. 1b, S7 and Note S1†), the Cu-only sample displayed a faradaic efficiency (FE) of 31% towards $H_2$, while the FE to $C_{2+}$ products was 54%. Among the $C_{2+}$ products, ethylene, ethanol, and acetate were formed with FEs of 13%, 12%, and 17%, respectively. Such a product distribution is typical for Cu electrocatalysts measured under alkaline conditions.[38,39] Increasing the Ag content up to 5 mol% in the $Cu_{0.95}Ag_{0.05}$ sample did not significantly influence the FEs, as a similar product distribution was observed compared to the Cu-only catalyst. In contrast, adding 10 mol% of Ag suppressed $H_2$ and enhanced the $C_{2+}$ product formation, leading to FEs of 23% and 63%, respectively, for the $Cu_{0.9}Ag_{0.1}$ sample. The FE to propanol, in particular, reached a high value of 18% for this composition. Among recent CORR works, only the groups of Sargent and Jiao reported high propanol FE on Cu–Ag bime-tallic catalysts.[12,38] Most of the literature, however, reported a propanol FE below 5%,[11,19,39] revealing the challenging nature of chain growth during CORR. The $C_{2+}$ product FE decreased with increasing further the Ag content, with FEs of 59% and 48% for $Cu_{0.75}Ag_{0.25}$ and $Cu_{0.5}Ag_{0.5}$, respectively (Fig. 1c). The Ag-only catalyst produced only $H_2$, showing the negative impact of high Ag content on $C_{2+}$ formation. For completeness, the minor side-products formed on all samples are shown in Fig. S6.†

The Cu-only and $Cu_{0.9}Ag_{0.1}$ samples were also tested at two other potentials, namely −0.5 V and −0.6 V *vs.* RHE (Fig. S8†). The comparison of these two samples at these more negative potentials emphasized the selectivity trends discussed before. At potentials of −0.5 V and −0.6 V *vs.* RHE, $Cu_{0.9}Ag_{0.1}$ demonstrated a higher selectivity to $C_{2+}$ products than the Cu-only sample. The $C_{2+}$ product FE reached 45% on $Cu_{0.9}Ag_{0.1}$, whereas it declined to 28% for Cu-only at −0.6 V *vs.* RHE. Our data suggest that different active sites are present in the $Cu_{0.9}Ag_{0.1}$ and Cu-only samples and that the presence of Cu–Ag interactions in the former catalyst benefits C–C coupling reactions and suppresses the competing hydrogen evolution reaction (HER).

## 2.2. Comparison of sol–gel $Cu_{0.9}Ag_{0.1}$ with reference samples

The observed CORR selectivity trends point to a synergy between Cu and Ag for the $Cu_{0.9}Ag_{0.1}$ sample. To better understand the nature of the Cu–Ag interactions formed during sol–gel synthesis, the CORR performance of the $Cu_{0.9}Ag_{0.1}$ sample was compared to two reference samples of the same composition obtained by (i) galvanic exchange of Cu with Ag[38] and (ii) physical mixing of the Cu-only and Ag-only samples (Fig. 1d and S9†). Galvanic
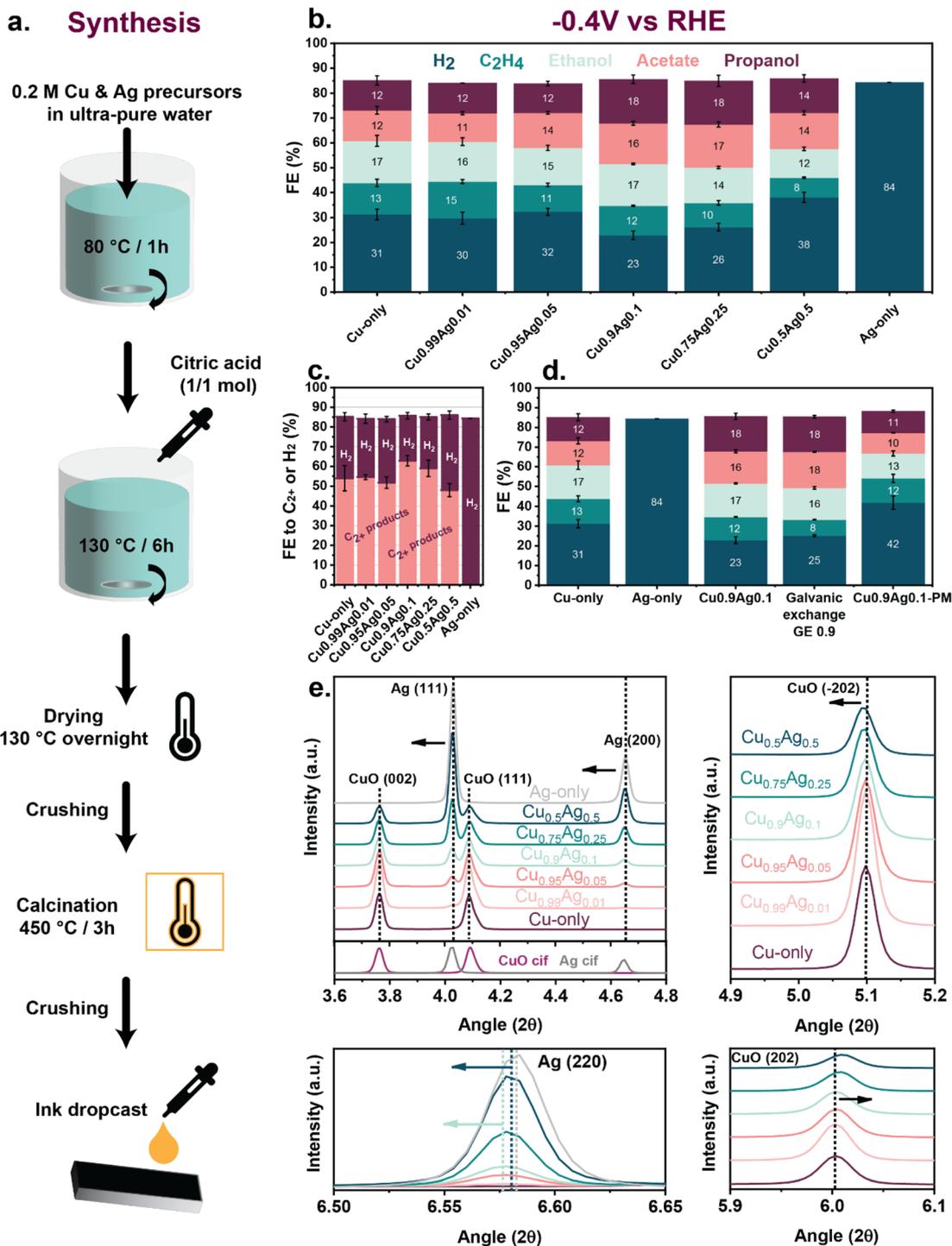
Fig. 1 (a) Sol−gel synthesis method employed to prepare bimetallic Cu−Ag, Cu-only and Ag-only samples, (b) faradaic efficiencies of the sol−gel samples measured at −0.4 V vs. RHE, CORR, 1 h, 3 M KOH, (c) faradaic efficiencies to $C_{2+}$ products and $H_2$ of the sol−gel samples measured at −0.4 V vs. RHE, CORR, 1 h, 3 M KOH, (d) Comparison of the faradaic efficiencies of the sol−gel and reference samples prepared by galvanic exchange and physical mixing measured at −0.4 V vs. RHE, CORR, 1 h, 3 M KOH, (e) X-ray diffractograms of the as-prepared samples (WAXS, $\lambda$ = 0.0165312 nm).

exchange can be used to synthesize bimetallic Cu–Ag catalysts with strong surface interactions, while physical mixing results in catalysts where the phases are physically isolated.[28,32,39,41] As the Ag atoms replace only the surface Cu atoms during galvanic exchange, it is not likely that Ag atoms would be present in the

bulk of the Cu phase. The surface composition of the galvanically exchanged reference (referred to as GE 0.9) was chosen to match the surface composition of $Cu_{0.9}Ag_{0.1}$ after reduction based on quasi-in situ XPS data, and the synthesis parameters were adapted accordingly (Table S7†). The physically mixed sample

This journal is © The Royal Society of Chemistry 2025

J. Mater. Chem. A, 2025, 13, 2285–2300 | 2287

(referred to as $Cu_{0.9}Ag_{0.1}$-PM) was prepared by mixing the Cu-only and Ag-only samples, both obtained by sol–gel synthesis, in the appropriate ratio. The product distribution of $Cu_{0.9}Ag_{0.1}$-PM, at −0.4 V vs. RHE, resembled the one of the Cu-only sample (Fig. 1d). The increase in $H_2$ production can be explained by the presence of separate Ag particles and the absence of synergetic interactions between the Cu and Ag phases. More importantly, the $Cu_{0.9}Ag_{0.1}$ and GE 0.9 displayed a similar FE for oxygenates, i.e., 49% and 52%, respectively. Based on this observation, we speculate that the Cu–Ag interactions in $Cu_{0.9}Ag_{0.1}$ resemble those in GE 0.9, suggesting the formation of a surface Cu–Ag nanoalloy in $Cu_{0.9}Ag_{0.1}$.[32,42]

### 2.3. Cu–Ag interactions in the as-prepared samples

Ex situ wide-angle X-ray scattering (WAXS) was employed to determine the crystalline phase composition and crystallite size of the as-prepared samples. The as-synthesized samples comprised monoclinic CuO and face-centered cubic (fcc) metallic Ag phases (Fig. 1e and S13a†).[36,43–45] The shift of all Ag reflections to lower diffraction angles in the Cu–Ag bimetallic samples indicated an expansion of the Ag lattice compared to the Ag-only reference (Table S4 and Fig. S14†). The largest shift of the Ag (220) and (200) reflections was observed for Ag contents of 5 and 10 mol%. Furthermore, some CuO reflections in the bimetallic samples shifted to higher angles (e.g., CuO

(110), CuO (002), CuO (202)) and lower angles (e.g., CuO (−202)), pointing to CuO lattice distortions (Fig. S14†). These observations demonstrate a prominent effect of the bulk composition on the monoclinic CuO and fcc Ag lattice parameters.

Similarly, the surface speciation of the samples investigated by XPS depended strongly on the composition (Fig. 2a and S17a†). The XPS spectrum of the Ag-only sample was characteristic of metallic Ag (Ag $3d_{5/2}$ binding energy (BE) at 368.2 eV,[46,47] spin–orbit splitting 6 eV (ref. 46)), and the presence of plasmon features indicated the presence of large Ag particles.[48] The Ag 3d spectra of $Cu_{0.5}Ag_{0.5}$ and $Cu_{0.75}Ag_{0.25}$ resembled the spectrum of the Ag-only sample and plasmon features were present, confirming the large size of metallic Ag domains in these samples. At lower Ag content ($Cu_{0.9}Ag_{0.1}$), Ag species were present as a mixture of metallic Ag and $AgO_x$ (Ag $3d_{5/2}$ BE at 367.0 eV).[49] The absence of plasmon features implies that the Ag particles in $Cu_{0.9}Ag_{0.1}$ are relatively small. Decreasing the Ag content further led to the formation of small Ag clusters in $Cu_{0.95}Ag_{0.05}$ (Ag $3d_{5/2}$ BE at 369.5 eV (ref. 50)) and a nearly fully oxidized surface in $Cu_{0.99}Ag_{0.01}$. In samples containing less than 10 mol% Ag, the formation of $AgO_x$ next to metallic Ag shows the abundance of small Ag domains, which are readily oxidized. A high Ag dispersion implies an increasing number of CuO–Ag interfaces. Cu–Ag interfaces have been reported to enhance the $C_{2+}$ product selectivity.[37,39] The Cu $2p_{3/2}$ spectra of all samples
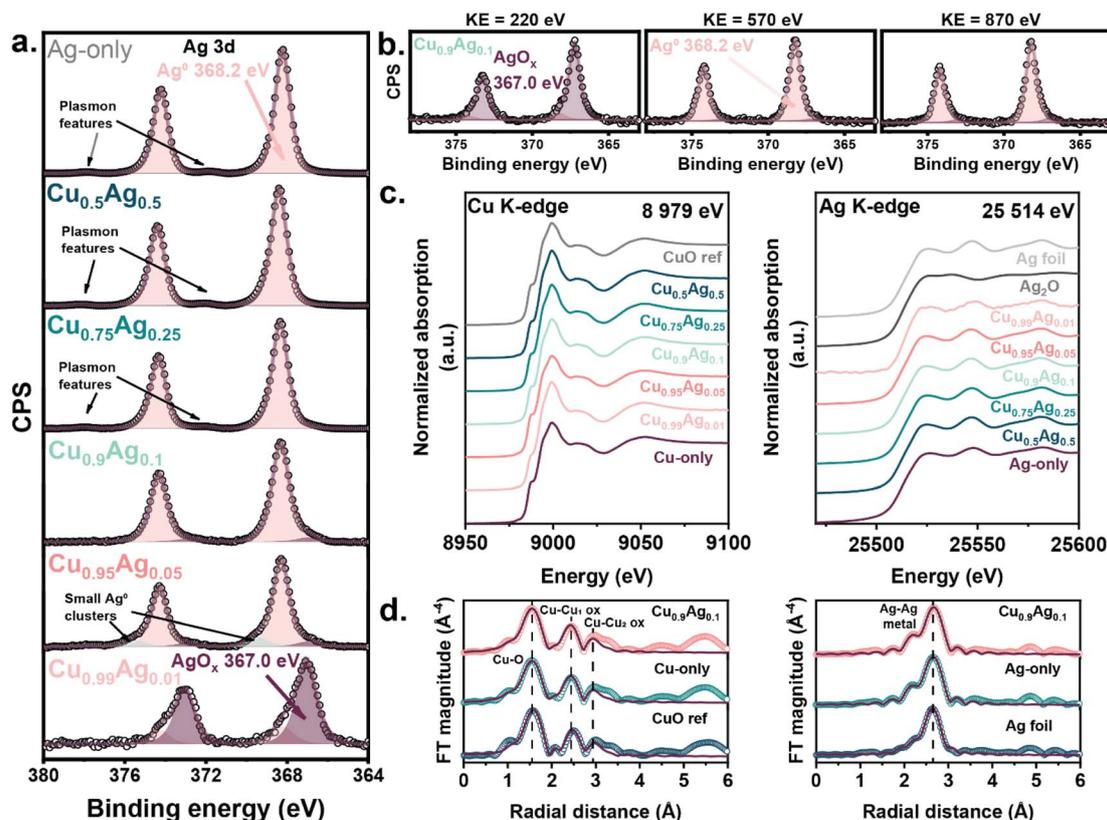


Fig. 2 (a) XPS spectra of the as-prepared samples (monochromatic Al Kα = 1486.6 eV), (b) depth profile of $Cu_{0.9}Ag_{0.1}$ measured by synchrotron-based XPS at various kinetic energies, (c) Cu K-edge XANES and Ag K-edge XANES spectra of the as-prepared samples, and (d) Cu and Ag $k^3$-weighted FT-EXAFS of the as-prepared samples.

displayed the characteristic features of CuO (Cu $2p_{3/2}$ BE at 933.5 eV, satellite features from 940–945 eV) (Fig. S17a†). The area ratio of the main line and the satellite was equal to 2, which confirms the sole presence of $Cu^{2+}$.[51]

The speciation of Ag at the surface was further investigated using synchrotron-based XPS (Fig. 2b). As the inelastic mean free path of the emitted photoelectrons depends on their kinetic energy, the possibility of tuning the energy of the incoming X-rays allows measuring at various depths of the surface layer. At low excitation energy, only photoelectrons originating from atoms at the very surface have sufficient kinetic energy to escape the sample (kinetic energy, KE = 220 eV). Increasing the excitation energy leads to probing atoms located deeper in the layer, for which 570 and 870 eV kinetic energies were used. By selecting different excitation energies, we could probe Cu and Ag at the same kinetic energy, meaning the atoms were located at the same depth (Fig. S17c†). At KE = 220 eV, the surface region of the $Cu_{0.9}Ag_{0.1}$ sample was mainly composed of $AgO_x$ (Ag $3d_{5/2}$ BE at 367.0 eV) and only a small amount of metallic Ag (Ag $3d_{5/2}$ BE at 368.2 eV (ref. 49)). Conversely, the $Cu_{0.75}Ag_{0.25}$ and $Cu_{0.5}Ag_{0.5}$ samples did not display any oxidized Ag species at KE = 220 eV, with the spectra being dominated by metallic Ag species (Fig. S17b†). In line with the lab-based XPS, the plasmon features in the spectra of $Cu_{0.75}Ag_{0.25}$ and $Cu_{0.5}Ag_{0.5}$ confirmed the presence of large metallic Ag particles.[48] These data suggest that the Ag domains in $Cu_{0.9}Ag_{0.1}$ are smaller and better dispersed than in samples containing more Ag. At greater depths, KE of 570 and 870 eV, the $Cu_{0.9}Ag_{0.1}$ sample displayed a prominent metallic Ag signal and a small amount of $AgO_x$ (Fig. 2b). The absence of plasmon features and the presence of oxidized species at all tested KEs confirmed that small and dispersed Ag domains are present at the surface of $Cu_{0.9}Ag_{0.1}$. In contrast, large Ag particles are present in samples containing a higher Ag content.[48] Moreover, the atomic percentage of Ag in $Cu_{0.9}Ag_{0.1}$ at shallow depths (KE 220 eV) was higher than in deeper locations, which correlates with the high dispersion of the Ag phase (Fig. S17c†).

The lattice parameters of the monoclinic CuO and fcc Ag phases were determined by Rietveld refinement of the WAXS data. As-prepared $Cu_{0.9}Ag_{0.1}$ showed larger CuO lattice parameters than the other samples (Fig. S15, 16 and Table S9†). In agreement with the peak shift discussed earlier, the Ag lattice was the most expanded in Cu–Ag samples containing less than 10 mol% Ag. The expansion of the Ag lattice seen by WAXS cannot be explained by the substitution of Ag (atomic radius 144 pm) with metallic Cu (atomic radius 128 pm).[52] Instead, we attribute this to the formation of an interfacial phase between the metallic Ag domains and the oxidized CuO domains. The formation of Cu–Ag mixed oxides (e.g. $AgCuO_2$ or $Ag_2Cu_2O_3$) at the interface of oxidized CuO and reduced Ag phases has been discussed before.[53,54] Due to the similar atomic arrangement of the CuO ($-111$) and $Cu_4O_3$ (202) planes,[55] it has been suggested that CuO is modified into a $Cu_4O_3$-like structure along the ($-111$) plane, which is able to form such mixed oxides with Ag.[19,47,56] These modifications also impact the CuO lattice parameters as evidenced by Rietveld refinement (Fig. S15, 16 and Table S9†). Moreover, the oxidation of Ag domains at the

CuO–Ag interface (Cu–Ag mixed oxides), also evidenced by XPS, is likely responsible for the increase in fcc Ag lattice parameter. In support of this, diffractograms of samples with low Ag content (e.g., $Cu_{0.95}Ag_{0.05}$, Fig. S13b†) were found to contain traces of another Cu-containing phase, corresponding to either cubic CuO or a Cu–Ag mixed oxide phase (e.g. $AgCuO_2$ or $Ag_2Cu_2O_3$).[47,56,57] The occurrence of cubic CuO is unlikely as this phase does not exist naturally and has rarely been successfully synthesized.[57] Thus, based on WAXS and XPS data, we believe that the formation of Cu–Ag mixed oxides at the interface between the Ag and CuO phases caused the changes in peak positions and lattice parameters in the Cu–Ag bimetallic samples, especially in samples with low Ag content ($\leq$10 mol%).

X-ray absorption near-edge spectroscopy (XANES) at the Cu and Ag K-edges was employed to probe the bulk oxidation state of the as-prepared samples. $Cu^{2+}$ from CuO and metallic Ag were observed in line with the other characterization methods (Fig. 2c).[40,58,59] The local environment of Cu and Ag was investigated by analyzing the extended X-ray absorption fine structure (EXAFS) region of the XAS spectra (Fig. 2d), which agreed with the presence of CuO[60] and Ag.[61] The coordination number of Ag increased from 8.8 $\pm$ 0.6 for the $Cu_{0.99}Cu_{0.01}$ sample to 11.9 $\pm$ 0.4 for the Ag-only sample, in agreement with the different Ag dispersion noted above (Table S5†).

HAADF-STEM images and EDX mapping (Fig. 3 and S18†) showed that all as-prepared samples contained CuO particles, ranging from a few hundred nanometers to sub-micrometer size regardless of the Ag content. On the contrary, the Ag dispersion strongly depended on the Ag content. In the $Cu_{0.5}Ag_{0.5}$ sample, Ag was predominantly present as 100–500 nm particles. In contrast, the $Cu_{0.95}Ag_{0.05}$ and $Cu_{0.9}Ag_{0.1}$ samples also contained much smaller Ag particles measuring only a few nanometers (Fig. 3). It is reasonable to speculate that these smaller Ag particles are present due to CuO–Ag interactions. To support this, certain regions showed decoration of Ag particles by a shell of CuO, confirming the formation of interactions at the CuO–Ag interfaces during the synthesis of samples with low Ag content (Fig. S19†). These observations align with the XPS results, which showed the higher dispersion of Ag species at low Ag content. As expected, the surface replacement of Cu in the galvanically exchanged GE 0.9 sample led to strong Cu–Ag interaction and dispersed Ag atoms (Fig. S20†). As the catalytic performances of $Cu_{0.9}Ag_{0.1}$ and GE 0.9 are similar, we speculate that the Cu–Ag interfacial sites in $Cu_{0.9}Ag_{0.1}$ under CORR are similar to GE 0.9 and are crucial for forming $C_{2+}$ products.

## 2.4. Cu–Ag interactions during CORR

Although *ex situ* characterization provided insights into the CuO–Ag interactions in the as-prepared state of the sample, electroreduction can lead to phase transformations and very different morphologies, which can be best studied using *in situ* techniques.[34,40,42] We used quasi-*in situ* XPS to investigate the surface oxidation state and composition after the reduction of the samples at $-0.4$ V *vs.* RHE in 3 M KOH (Fig. 4a–d, S21a–c and Table S6†). These measurements were done in an XPS
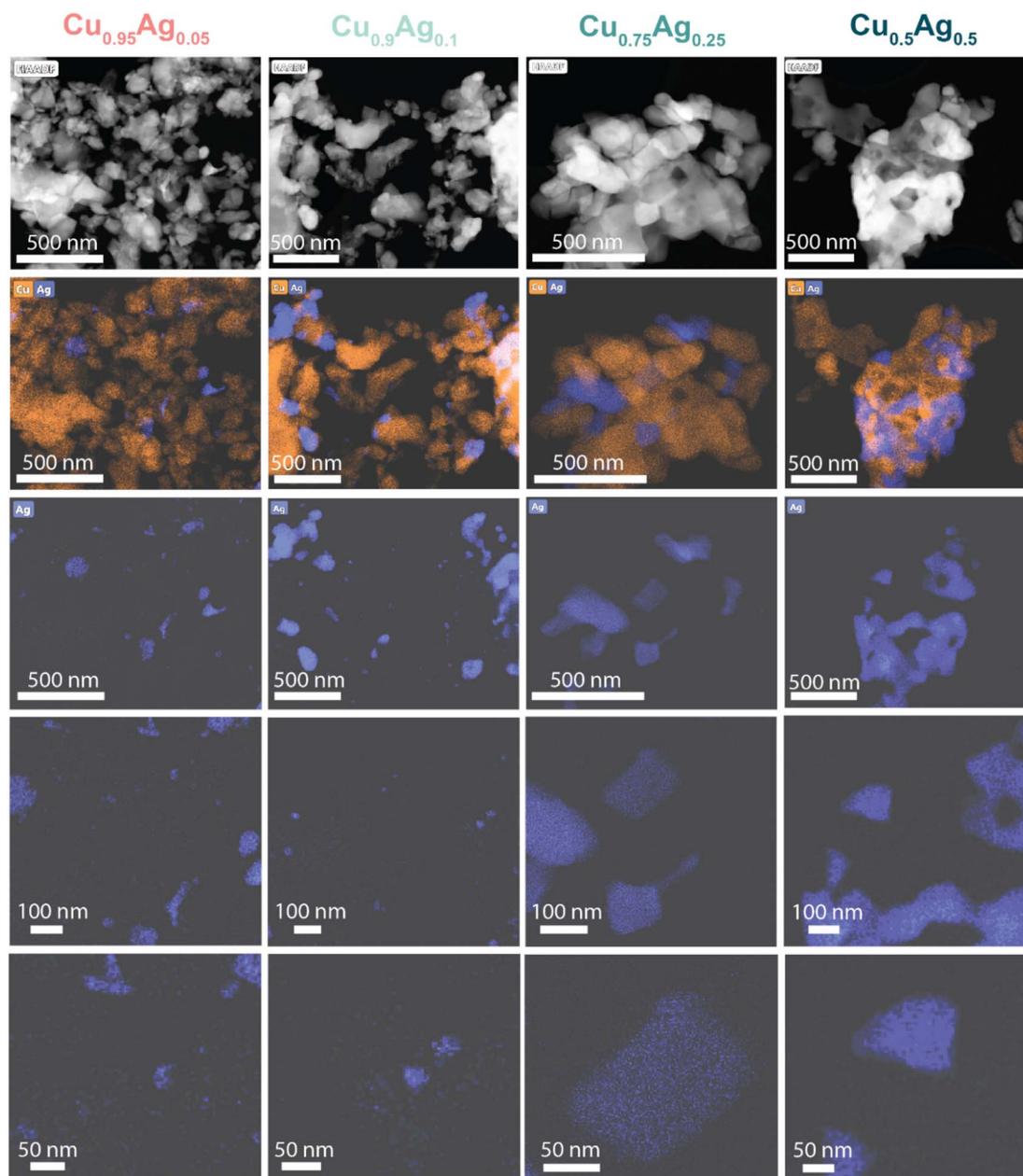
This journal is © The Royal Society of Chemistry 2025

*J. Mater. Chem. A*, 2025, **13**, 2285–2300 | **2289**

**Fig. 3** HAADF-STEM images and corresponding EDX maps of the as-prepared $Cu_{0.95}Ag_{0.05}$, $Cu_{0.9}Ag_{0.1}$, $Cu_{0.75}Ag_{0.25}$ and $Cu_{0.5}Ag_{0.5}$ samples.

system that allows transferring the samples from the electrochemical cell to the XPS analysis chamber under an inert atmosphere (He), preventing post-reaction oxidation by air exposure. The surface of all samples was fully reduced after 10 min of reduction at −0.4 V vs. RHE (Fig. 4a–d and S21†), as shown by the Cu $2p_{3/2}$ line at BE 932.5 eV, the Cu LMM Auger line shape, the Ag $3d_{5/2}$ line at BE 368.2 eV and the Ag MNN Auger line shape.[51,56,62] The minor contribution of $Cu(OH)_2$ (Cu $2p_{3/2}$ line at BE 935.5 eV, satellite at BE 945 eV (ref. 51)) likely originates from the reaction of the sample with KOH upon drying or exposure to the open circuit potential (OCP).[63,64] $Cu_{0.5}Ag_{0.5}$ and $Cu_{0.75}Ag_{0.25}$ were composed of large Ag domains, as follows from the plasmon features.[48] The absence of such features in the spectra of $Cu_{0.9}Ag_{0.1}$ and $Cu_{0.95}Ag_{0.05}$ showed that these samples contained much smaller Ag domains than samples with a high Ag content. The surface Ag/Cu ratio in $Cu_{0.9}Ag_{0.1}$ decreased during the reduction (Table S6†) and was the lowest among the investigated samples. The low surface Ag content and the high dispersion of the Ag domains in $Cu_{0.9}Ag_{0.1}$ points to the abundance of Cu–Ag interfacial sites. These interfaces are thought to induce electronic effects between Cu and Ag, modifying the binding strength of intermediates relevant to $C_{2+}$ product formation and, hence, the selectivity to such products.[37–39] This can explain the more significant formation of $C_{2+}$ products on the $Cu_{0.9}Ag_{0.1}$ sample.

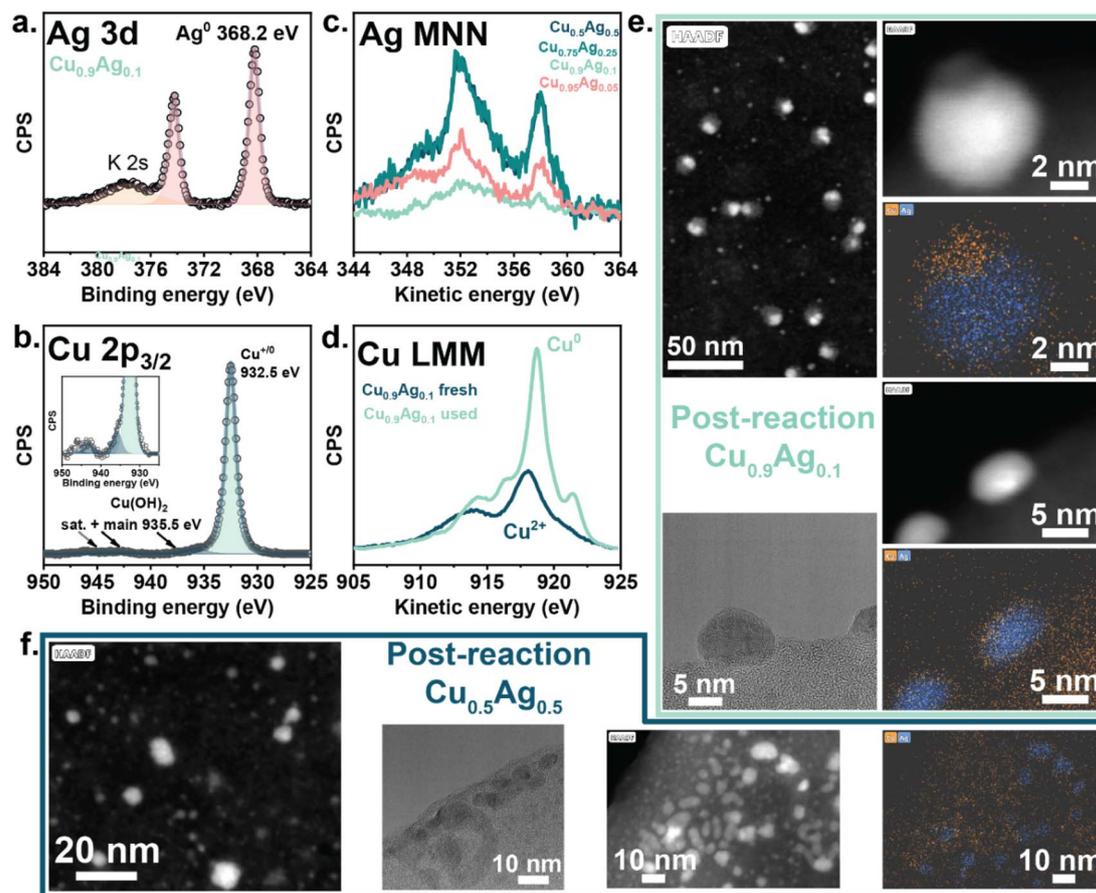**2290** | *J. Mater. Chem. A*, 2025, **13**, 2285–2300

This journal is © The Royal Society of Chemistry 2025

**Fig. 4** Quasi-*in situ* XPS spectra of the (a) Ag 3d and (b) Cu 2p$_{3/2}$ lines of Cu$_{0.9}$Ag$_{0.1}$ after chronoamperometry at $-0.4$ V *vs.* RHE for 10 min, (c) Quasi-*in situ* XPS spectra of the Ag MNN lines of several Cu–Ag samples after chronoamperometry at $-0.4$ V *vs.* RHE for 10 min, (d) Quasi-*in situ* XPS spectra of the Cu LMM lines of Cu$_{0.9}$Ag$_{0.1}$ before and after chronoamperometry at $-0.4$ V *vs.* RHE for 10 min, (e) and (f) HAADF-STEM images and EDX maps of used (e) Cu$_{0.9}$Ag$_{0.1}$ and (f) Cu$_{0.5}$Ag$_{0.5}$ after CORR at $-0.4$ V *vs.* RHE, 1 h, 3 M KOH.

HAADF-STEM and EDX mapping revealed a composition-dependent reorganization of Cu and Ag phases during CORR (Fig. 4e–f and S22†). Contrasting with the dimensions of the as-prepared samples, the used Cu$_{0.9}$Ag$_{0.1}$ and Cu$_{0.5}$Ag$_{0.5}$ samples contained particles measuring less than 20 nm. After the reaction, Cu$_{0.9}$Ag$_{0.1}$ comprised 2–15 nm Cu–Ag bimetallic particles with an off-centered core–shell structure.[65,66] Such morphologies give rise to extended Cu–Ag interfaces, which correlates with the XPS results. The Z-contrast HAADF-STEM and EDX-mapping revealed that Ag resides in the core of polycrystalline particles, while Cu was predominantly present in the shell. We should note that in Cu$_{0.9}$Ag$_{0.1}$, the Ag–Cu core–shell structures coexisted with ~3 nm Cu particles, seemingly not interacting with Ag. Conversely, the used Cu$_{0.5}$Ag$_{0.5}$ was predominantly composed of separate metallic Cu and Ag particles and only a small fraction of core–shell structures. The presence of extended Cu–Ag interfaces in Cu$_{0.9}$Ag$_{0.1}$ can explain the enhanced selectivity to C$_{2+}$ products, while H$_2$ predominantly evolves on separated phases in the Cu$_{0.5}$Ag$_{0.5}$ sample.[38,39] The microscopy data of the used GE 0.9 sample revealed that many Cu–Ag interfaces were present after CORR (Fig. S23†). We believe that the nature of Cu–Ag interactions at the interface between the Ag-core and the Cu-shell in Cu$_{0.9}$Ag$_{0.1}$ is similar to

the interactions found in the GE 0.9 sample, explaining their similar catalytic performance.

Under CORR conditions, the reduction of the parent CuO and dissolution–redeposition processes can result in the restructuring of the Cu phase.[67–69] The restructuring of metallic Ag was less expected as the phase remained identical. The size of Ag particles decreased drastically during CORR compared to the as-prepared domains. Yun *et al.* studied the morphological changes of Ag nanoparticles by *in situ* TEM under CO2RR conditions.[70] The authors demonstrated that the metallic Ag particles decreased in size during the first instances of reduction and subsequently redispersed following a dissolution–redeposition process. As the final structure of the sol–gel-derived samples varied with their composition, it is important to also characterize the reduced samples.

X-ray absorption spectroscopy (XAS) was utilized to probe structural and redox transformations during CORR while simultaneously monitoring gaseous products by mass spectrometry. To mimic the experimental protocol used before catalytic testing, cyclic-voltammetry cycles (+0.5 V to $-0.6$ V *vs.* RHE, 5 mV s$^{-1}$) were recorded while the cell was flushed with N$_2$ in a flow-by mode. During the first CV cycle, all samples underwent partial or total reduction from CuO to metallic Cu

This journal is © The Royal Society of Chemistry 2025

*J. Mater. Chem. A*, 2025, **13**, 2285–2300 | **2291**

(Fig. 5a, b, S25–26, S28 and S29†).[58,71] The presence of isosbestic points indicated a direct reduction from CuO to Cu without the formation of $Cu_2O$ (Fig. S24†). Therefore, linear combination fitting was applied using only CuO and Cu references to quantify the reduction of each sample. After the first CV, the $Cu_{0.9}Ag_{0.1}$ sample was completely reduced, unlike the Cu-only sample (71% $Cu^0$). The CV recorded in $N_2$ and CO demonstrated that the onset of CuO reduction occurred at lower potentials on $Cu_{0.9}Ag_{0.1}$ compared to Cu-only (Fig. S1 and 2†), indicative of synergistic interactions between Cu and Ag in the

bimetallic sample. These interactions facilitate the reduction of CuO to Cu. The dependence of the reducibility of CuO on the Ag content has earlier been associated with Cu–Ag interfacial sites.[72] In the subsequent CV cycles (Fig. S25–28 and S30†), the oxidation state of the Cu species was stable in all samples. Similarly, the Ag species remained metallic upon cycling (Fig. S29c†).

Next, CORR was carried out on each sample at −0.4 V vs. RHE and −0.6 V vs. RHE (Fig. 5c–f, S31–34 and Table S8†). During these measurements, the $Cu_{0.9}Ag_{0.1}$ sample only
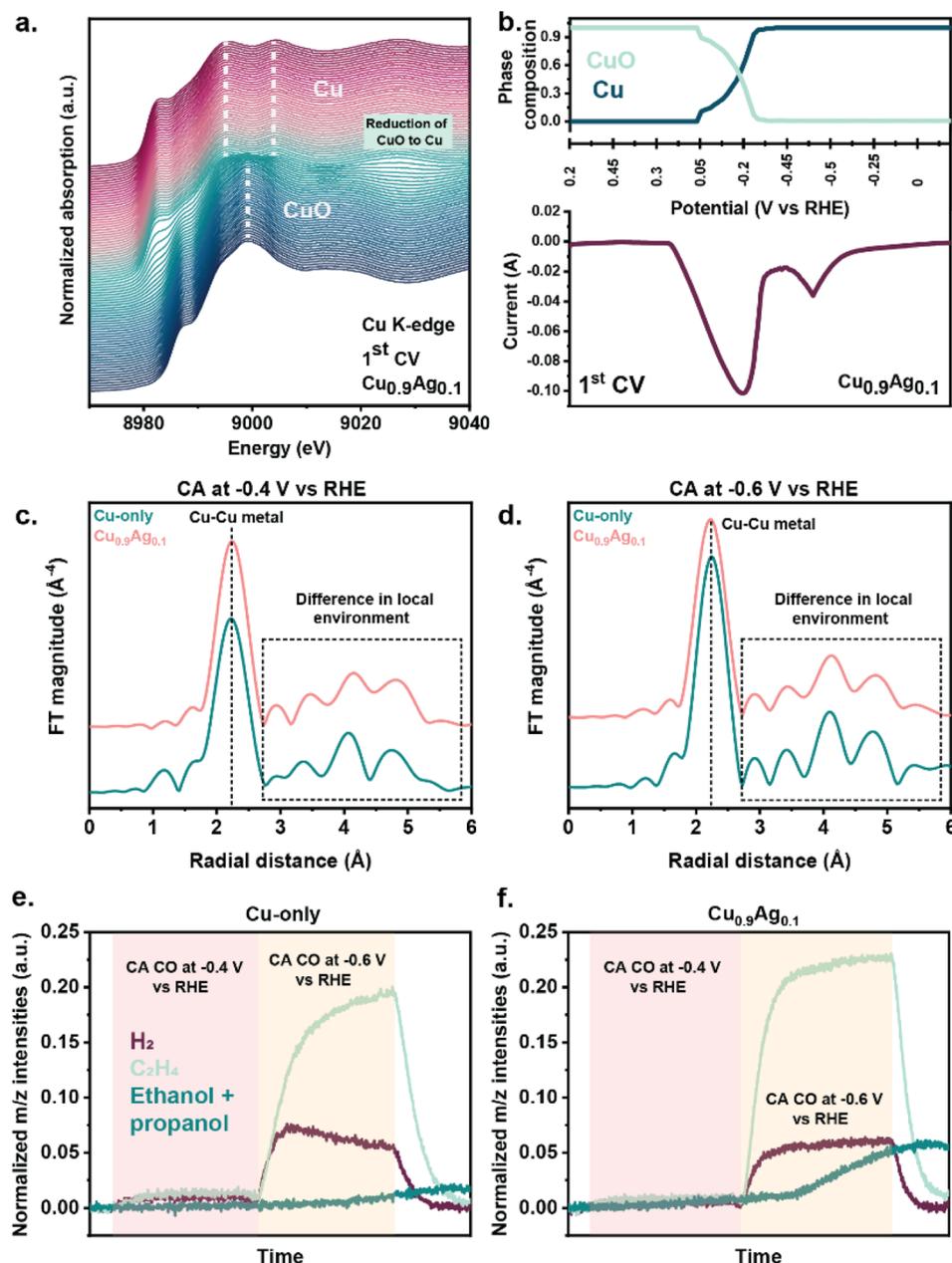


Fig. 5 (a) Cu K-edge XANES spectra of $Cu_{0.9}Ag_{0.1}$ during the first CV measurement, 3 M KOH, start +0.2 V vs. RHE, cycle from +0. 5 V to −0.6 V vs. RHE, 5 mV s$^{-1}$, (b) linear combination fitting of spectra recorded during the first CV of $Cu_{0.9}Ag_{0.1}$ and the CV signal, 3 M KOH, start +0.2 V vs. RHE, cycle from +0.5 V to −0.6 V vs. RHE, 5 mV s$^{-1}$, (c) Cu $k^3$-weighted FT-EXAFS of Cu-only and $Cu_{0.9}Ag_{0.1}$ recorded during the CA at −0.4 V vs. RHE, (d) Cu $k^3$-weighted FT-EXAFS of Cu-only and $Cu_{0.9}Ag_{0.1}$ recorded during the CA at −0.6 V vs. RHE, (e) and (f) normalized $m/z$ intensities of $H_2$, $C_2H_4$, and ethanol + propanol MS signals measured during CA at −0.4 and −0.6 V vs. RHE of (e) Cu-only and (f) $Cu_{0.9}Ag_{0.1}$ (normalization on the CO $m/z$ intensity).

contained metallic Cu and Ag species, while the reduction of the Cu-only sample was only complete at the end of the chronoamperometric experiment at −0.6 V $vs.$ RHE (Fig. S31 and S33†). The Cu $k^3$-weighted FT-EXAFS showed that, despite the similar metallic Cu–Cu first coordination shell, the Cu-only and $Cu_{0.9}Ag_{0.1}$ samples exhibited significantly different coordination environments at longer radial distances (Fig. 5c and d). The differences observed in the Cu $k^3$-weighted FT-EXAFS of $Cu_{0.9}Ag_{0.1}$ likely arise from Cu–Ag interactions. Mass signals ($m/z$) of products were followed during the $operando$ XAS measurements. $Cu_{0.9}Ag_{0.1}$ showed the largest normalized $m/z$ intensities for ethylene, ethanol, and propanol (Fig. 5e and f), correlating with the highest $C_{2+}$ product FE measured during CORR. As the $operando$ XAS data confirmed that Cu species in $Cu_{0.9}Ag_{0.1}$ were exclusively present in the metallic state during CORR, the enhanced $C_{2+}$ product selectivity measured on this sample did not originate from traces of $Cu^{\delta+}$, as suggested for Cu-based electrocatalysts in earlier works.[33,40] Instead, the analysis of the local environment of Cu atoms in $Cu_{0.9}Ag_{0.1}$ revealed Cu–Ag interactions during CORR, which correlate with higher normalized $m/z$ intensities of the $C_{2+}$ products. This strongly suggests that the higher $C_{2+}$ product selectivity can be explained by CORR reactions at Cu–Ag interfacial sites.

$In situ$ WAXS was employed to understand the transformations of the crystalline phases upon reduction and CORR. During a first cyclic-voltammogram (CV from +0.3 V to −0.3 V $vs.$ RHE, 2 mV s$^{-1}$, N$_2$ atmosphere), the Ag-containing samples displayed the complete reduction of crystalline CuO to metallic Cu (Fig. 6a and S35†). At peak cathodic currents, the Cu (111) and (200) reflections were visible in the diffractograms and their integral intensities kept increasing upon subsequent cycling.[73] In contrast, the Cu reduction was incomplete for the Cu-only sample (Fig. S35†). Similarly to the XAS results, $in situ$ WAXS showed that the presence of Ag promoted the reduction of CuO to Cu. As expected, the metallic Ag crystallites in the precursor remained metallic upon cycling. However, the crystallite sizes and the positions of the reflections changed when a negative potential was applied (Fig. 6a–c and S35†). For instance, the crystallite size of Ag (derived from the (220) reflection) in the $Cu_{0.9}Ag_{0.1}$ sample decreased from 28 to 23 nm (5 nm) when CuO was reduced to metallic Cu. The Ag domain size stabilized once the reduction of CuO was completed, serving as another indication for CuO–Ag interactions (Cu–Ag mixed oxides) in the as-prepared samples. The largest Ag crystallite size difference was observed for $Cu_{0.95}Ag_{0.05}$ (~7 nm) and the smallest for $Cu_{0.5}Ag_{0.5}$ (~2 nm) (Fig. 6c).



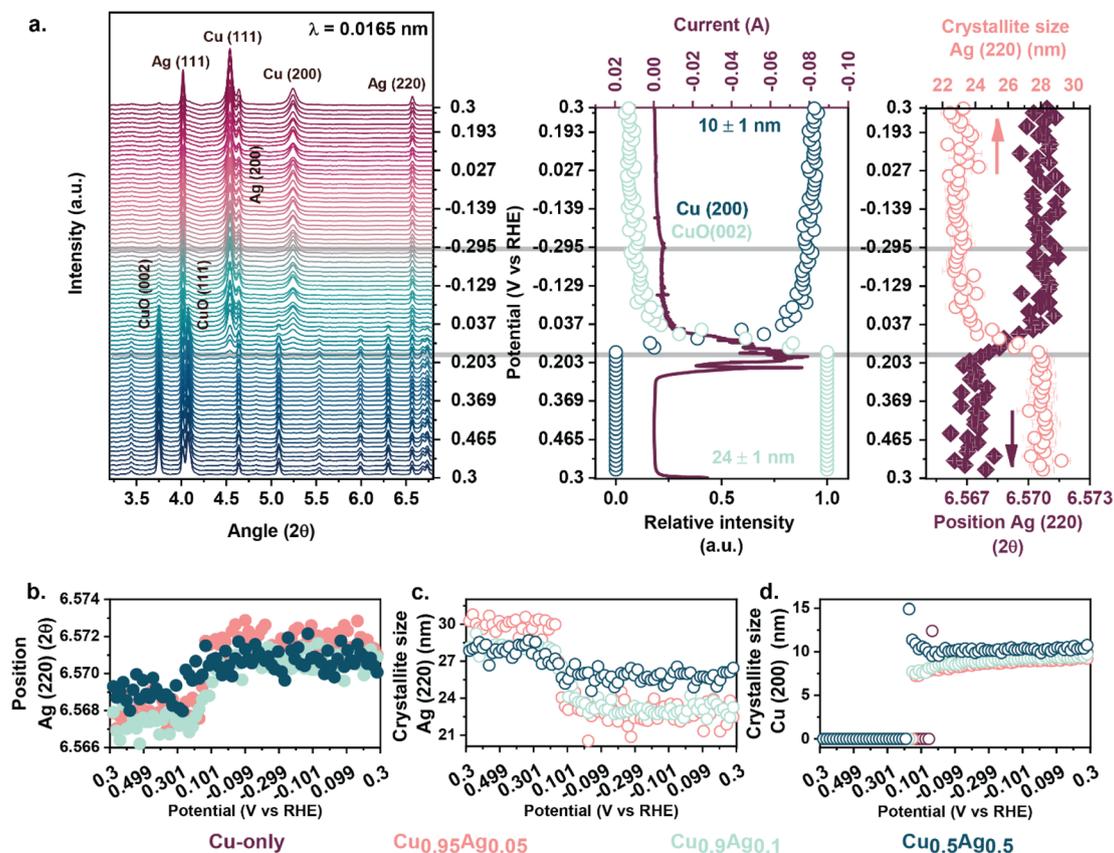**Fig. 6** (a) $In situ$ WAXS of $Cu_{0.9}Ag_{0.1}$ during the first CV cycle (3 M KOH, start +0.3 V $vs.$ RHE, cycle from +0.5 V to −0.3 V $vs.$ RHE, 2 mV s$^{-1}$) (left panel), corresponding CV and relative intensity of the CuO (002) and Cu (200) reflections recorded during the CV (middle panel), evolution of the Ag crystallite size and peak position of Ag (220) during the CV (right panel), (b) evolution of the Ag crystallite size derived from the Ag (220) reflection, (c) evolution of the peak position of Ag (220) and (d) evolution of the Cu crystallite size derived from the Cu (200) reflection for several Cu–Ag bimetallic and Cu catalysts recorded during the first CV (3 M KOH, start +0.3 V $vs.$ RHE, cycle from +0.5 V to −0.3 V $vs.$ RHE, 2 mV s$^{-1}$).

This journal is © The Royal Society of Chemistry 2025

J. Mater. Chem. A, 2025, **13**, 2285–2300 | **2293**

Additionally, the position of the Ag (220) reflection, initially displaced at lower angles compared to the Ag-only sample, shifted back to higher angles upon reduction (Fig. 6b). This shift occurred simultaneously with the loss of CuO reflections, further supporting the strong interactions between the two phases and the presence of mixed oxides in the as-prepared catalysts. The difference between the initial and final peak positions ($\Delta 2\theta$) was smaller at a high Ag content ($Cu_{0.5}Ag_{0.5}$; $\Delta 2\theta = 0.00124°$) than at a low Ag content ($Cu_{0.9}Ag_{0.1}$; $\Delta 2\theta = 0.0045°$), indicating more numerous CuO–Ag interfaces in the latter case. The catalysts were further analyzed over several cyclic voltammograms (+0.3 V to −0.4 V $vs.$ RHE, 2 mV s$^{-1}$, N$_2$ atmosphere). After 4 CV cycles, all catalysts were fully reduced (Fig. S36†). Despite the observation of similar metallic Cu and Ag phases, differences in crystallite sizes and peak positions were observed between the samples. While the crystallite sizes of Cu (111), Cu (200), Ag (111), and Ag (220) increased with increasing Ag content, the positions of these reflections shifted to lower angles (Fig. S36 and S38†). The position shift of the Cu reflections can be explained by the expansion of the lattice parameter due to alloying with Ag. As bulk Cu and Ag are immiscible, only Cu–Ag nanoalloys can be formed.[34,74–77]

The CO electrochemical reduction, carried out at −0.4 V $vs.$ RHE in a CO-purged electrolyte, only caused minor structural changes (Fig. S37 and 38†). During 20 min of CORR, the crystallite size and position of the reflections of the Cu and Ag phases did not change. Thus, we conclude that CO had a limited impact on the restructuring of the bulk structure under the applied conditions. Rietveld refinement was performed on the diffractograms recorded at half-time of the total CA duration. The fcc Cu and Ag lattice parameters were influenced by the composition of the $in$ $situ$ analyzed samples (Fig. S39, 40, Table S9 and Note S3†). The Cu lattice parameter increased by 0.0021 Å for $Cu_{0.9}Ag_{0.1}$ and by 0.0012 Å $Cu_{0.5}Ag_{0.5}$ compared to the Cu-only sample (3.6117 Å). Strehle $et$ $al.$ reported that the Cu lattice parameter of Cu–Ag nanoalloy systematically increased with the addition of Ag.[78] As the $Cu_{0.9}Ag_{0.1}$ sample demonstrated the largest Cu lattice expansion, we speculate that the Cu phase hosted more Ag than the other samples. In line with the XPS and XAS results, this hypothesis also aligns with the finding that $Cu_{0.9}Ag_{0.1}$ contains many Cu–Ag interfacial sites, as observed in the Ag–Cu core–shell structure by STEM-EDX.

Rietveld refinement of the Ag phase showed a difference in unit cell parameters between as-prepared and reduced samples (Fig. S39 and Table S9†). Upon reduction, the decrease of the Ag unit cell size was more significant at low Ag content, indicating that more Ag interacted with CuO in the as-prepared samples. During reduction, the Ag lattice parameter in the $Cu_{0.9}Ag_{0.1}$ (4.0824 Å) and $Cu_{0.5}Ag_{0.5}$ (4.0822 Å) samples approached the one of Ag-only (4.0823 Å), while the lattice parameter of $Cu_{0.95}Ag_{0.05}$ was instead lower (4.0803 Å). This contraction could be due to the inclusion of Cu atoms in Ag domains near the Cu–Ag interface.[78,79] These effects are more evident at low Ag content due to the low abundance of isolated Ag domains, in which Cu does not influence the Ag crystals. Previously, Jian $et$ $al.$ investigated how composition impacts the crystallographic and electronic properties of Cu–Ag solid solutions

(nanoalloys).[79] Replacing the Ag atoms with Cu resulted in lattice contraction. An Ag-rich solid solution displayed a lattice parameter close to pure Ag, while a Cu-rich sample exhibited a lattice parameter close to pure Cu. The Ag lattice contraction observed in $Cu_{0.95}Ag_{0.05}$ demonstrates that a significant amount of Cu is included in the Ag domains. Yet, the relatively small amount of such sites at 5 mol% Ag content did not improve the FE to C$_{2+}$ products compared to the Cu-only sample. The lattice parameters of Cu and Ag in $Cu_{0.5}Ag_{0.5}$ resembled those of the corresponding pure metals, which indicates the abundance of separate Cu and Ag domains. While only minor differences in Ag unit cell parameters were found in $Cu_{0.9}Ag_{0.1}$, the Cu lattice expanded the most in this sample, hinting at high Ag substitution levels due to the formation of abundant Cu–Ag nanoalloys in agreement with the XPS and XAS results. Cu–Ag nanoalloys at the interface between the Cu-shell and the Ag-core led to enhanced C$_{2+}$ product selectivity during CORR for the $Cu_{0.9}Ag_{0.1}$ sample.

## 2.5. The role of Cu–Ag interactions in CORR

Two main hypotheses concerning the nature of the active sites in bimetallic Cu–Ag catalysts for CORR to C$_{2+}$ products have been discussed. The first postulates that partial oxidation of Cu surfaces enhances the C$_{2+}$ product selectivity.[40,77] The presence of Ag can stabilize Cu$^{\delta+}$ species at the Cu surface upon reduction. The higher binding strength of CO on Cu$^+$ than on Cu is thought to increase the residence time of the reactant in the double layer, enhancing C$_{2+}$ formation through CO–CO coupling. Surface analysis by quasi-$in$ $situ$ XPS of our samples revealed the prevalence of metallic Cu at the surface under reducing conditions. Moreover, structural and compositional analysis by $in$ $situ$ WAXS and $operando$ XAS showed that oxidized Cu was absent during CORR. We also observed that Ag promoted the complete reduction of CuO to Cu. Therefore, we conclude that stabilizing oxidized Cu species by Ag cannot explain the improved product selectivity of the $Cu_{0.9}Ag_{0.1}$ sample. Alternatively, the promotional effect of Ag addition on C$_{2+}$ formation during CORR has been linked to a higher density of interfacial Cu–Ag sites.[19,32,39,80] The Cu–Ag interface forms a specific environment promoting the formation of Cu–Ag nanoalloys where electronic effects are concentrated. These affect the binding properties of reactants and intermediates, resulting in enhanced CO dimerization rates.[32,37–39,80] Our EDX mapping revealed the abundance of core–shell structures in bimetallic samples with a low Ag content ($Cu_{0.9}Ag_{0.1}$), while Cu and Ag particles were separated at high Ag concentration ($Cu_{0.5}Ag_{0.5}$). Moreover, the different peak positions observed by $in$ $situ$ WAXS indicated the formation of Cu–Ag nanoalloys, which were more abundant at low Ag content and likely located at the interface of the Cu and Ag domains in the core–shell structures. Rietveld refinement confirmed that the presence of Ag influenced the Cu lattice parameter measured during reduction and CORR. The largest Cu lattice expansion was measured for $Cu_{0.9}Ag_{0.1}$ and caused by the abundance of the Cu–Ag nanoalloys. The amount of such Cu–Ag interfacial sites depended on the Ag content. At very low Ag content (≤5 mol%),

the abundance of such nanoalloys is too low to improve the $C_{2+}$ product selectivity. The larger amount of such sites at an Ag content of 10 mol% promoted the formation of $C_{2+}$ products and suppressed HER. The high propanol faradaic efficiency (18% at $-0.4$ V *vs.* RHE) observed for the $Cu_{0.9}Ag_{0.1}$ sample likely originates from the abundant Cu–Ag nanoalloy sites, which facilitate not only $C_1$–$C_1$ but also $C_2$–$C_1$ coupling reactions. At high Ag content (50 mol%), the Cu and Ag phases are mostly separated, likely due to the predominant presence of separate CuO and Ag phases in the as-prepared sample and the low miscibility of Cu and Ag. We conclude that the physical separation of Cu and Ag phases is the primary cause of the selectivity shift from $C_{2+}$ products to $H_2$. Optimum Cu–Ag interactions were, therefore, obtained for the $Cu_{0.9}Ag_{0.1}$ sample.

Based on our WAXS data, it is reasonable to assume that the Cu–Ag interactions in the reduced catalysts strongly relate to the interactions between the CuO and Ag phases in the as-prepared samples formed during sol–gel synthesis. During sol–gel synthesis, the Cu and Ag atoms are homogeneously mixed at the atomic level in the gel.[81] We expect that the calcination of the gel results in the segregation of Ag from CuO due to their different affinities with oxygen.[82] Supported by XPS analysis, we contend that, at low Ag content, the segregated Ag atoms do not sinter into large particles, as these Ag species are highly dispersed in the solution. Instead, mixed oxides are formed at the CuO and Ag domains interface, likely stabilizing such small Ag particles. The presence of mixed oxides at the CuO–Ag interface indicates that the two phases are in close proximity. These mixed oxides are most likely the precursor for the Cu–Ag nanoalloys formed during CORR.[19] Conversely, the sintering of Ag into large particles is likely at high Ag content[83] which prevents the formation of mixed oxides at the interface with CuO. Moreover, EDX mapping before and after reduction pointed out some mobility of the Ag atoms despite remaining in the same oxidation state. Thus, although we believe that most of the Cu–Ag nanoalloy stems from the reduction of the mixed oxide in the interface region, the Cu–Ag nanoalloy may also originate from atom mobility during the reduction of the oxide precursors.[70] Such Cu–Ag nanoalloys were, however, not formed during the reaction in $Cu_{0.5}Ag_{0.5}$, which contained primarily separate CuO and Ag particles after sol–gel synthesis. The low miscibility of Cu and Ag may explain why nanoalloys are not formed from isolated phases during CORR.[34,74,75] Thus, we postulate that Cu–Ag nanoalloys, which benefit the $C_{2+}$ product selectivity, evolved predominantly from the reduction of initially interacting CuO and Ag phases (mixed oxides) synthesized by the sol–gel method.

## 3    Conclusion

Bimetallic Cu–Ag catalysts of different compositions were prepared by sol–gel synthesis and compared to Cu-only and Ag-only samples in CORR. The composition strongly influences the $C_{2+}$ product selectivity. While $Cu_{0.95}Ag_{0.05}$ did not improve the CORR performance compared to Cu-only, a Ag content of 10 mol% ($Cu_{0.9}Ag_{0.1}$) was optimal for forming $C_{2+}$ products. A higher Ag content promoted $H_2$ evolution, which competes with

C–C bond formation. $Cu_{0.9}Ag_{0.1}$ was compared to a reference sample GE 0.9 made by galvanic exchange containing surface Cu–Ag nanoalloys. Their CORR performances were similar, indicating similar active sites in both samples under reaction conditions. The as-prepared samples were predominantly composed of crystalline CuO and Ag phases, as shown by *ex situ* WAXS and XAS measurements. Nevertheless, the presence of mixed oxides (*e.g.*, $AgCuO_2$ or $Ag_2Cu_2O_3$) at the interface between CuO and Ag was indicated by WAXS data and further supported by HAADF-STEM images combined with EDX mapping. Mixed oxides were present at the CuO–Ag interface, especially at low Ag content ($\leq$10 mol%). Complementary XPS measurements revealed the partial oxidation of Ag species in these samples and a higher Ag dispersion than in samples containing more Ag, which confirms the abundance of CuO–Ag interfaces at low Ag content. Under electrochemically reducing conditions, these precursors underwent significant restructuring. Complete surface and bulk reduction were supported by quasi-*in situ* XPS, *in situ* WAXS, and *operando* XAS characterization. The presence of Ag promoted the complete reduction of CuO to Cu, as it was more challenging to reduce the Cu-only sample entirely. WAXS characterization showed the formation of Cu–Ag nanoalloys, next to crystalline Cu and Ag phases. The abundance of Cu–Ag nanoalloys was higher in $Cu_{0.9}Ag_{0.1}$ than in $Cu_{0.5}Ag_{0.5}$. Electron microscopy of used samples revealed that the Ag–Cu core–shell structures were abundant at low Ag content ($Cu_{0.9}Ag_{0.1}$) and scarce at high Ag content ($Cu_{0.5}Ag_{0.5}$), where mostly separated Cu and Ag particles were found. Therefore, the Cu–Ag nanoalloy phase observed in WAXS was likely located at the interface between the Ag-core and the Cu-shell of $Cu_{0.9}Ag_{0.1}$. The electronic effects present in the nanoalloys benefit C–C coupling. The presence of more Cu–Ag interfaces and the absence of separated Ag particles in $Cu_{0.9}Ag_{0.1}$ can explain the enhanced formation of $C_{2+}$ products. Conversely, the presence of separate Cu and Ag particles with few interfaces in $Cu_{0.5}Ag_{0.5}$ is detrimental to the selectivity to C–C coupling reactions during CORR, resulting in a higher selectivity to $H_2$. This study emphasizes the pivotal role of Cu–Ag nanoalloys in forming C–C bonds during CORR.

## Abbreviations

| | |
|---|---|
| CORR | CO electrochemical reduction reaction |
| CO2RR | $CO_2$ electrochemical reduction reaction |
| XPS | X-ray photoelectron spectroscopy |
| XAS | X-ray absorption spectroscopy |
| XANES | X-ray absorption near-edge spectroscopy |
| EXAFS | Extended X-ray absorption fine structure |
| STEM-EDX | Scanning transmission electron microscopy-Energy dispersive X-ray spectroscopy |
| HAADF-STEM | High-angle annular dark-field scanning transmission electron microscopy |
| ICP-OES | Inductively coupled plasma-optical emission spectroscopy |
| WAXS | Wide-angle X-ray scattering |
| OCP | Open circuit potential |

## Data availability

The authors confirm that the data supporting the findings of this study are available within the article and its ESI.†

## Author contributions

## Conflicts of interest

There are no conflicts to declare.

## Acknowledgements

## References

1 L. Wang, S. A. Nitopi, E. Bertheussen, M. Orazov, C. G. Morales-Guio, X. Liu, D. C. Higgins, K. Chan, J. K. Nørskov, C. Hahn and T. F. Jaramillo, Electrochemical Carbon Monoxide Reduction on Polycrystalline Copper: Effects of Potential, Pressure, and PH on Selectivity toward Multicarbon and Oxygenated Products, *ACS Catal.*, 2018, **8**(8), 7445–7454, DOI: 10.1021/acscatal.8b01200.

2 H. Zhang, J. Li, M.-J. Cheng and Q. Lu, CO Electroreduction: Current Development and Understanding of Cu-Based Catalysts, *ACS Catal.*, 2018, **9**, 49–65, DOI: 10.1021/acscatal.8b03780.

3 M. Jouny, G. S. Hutchings and F. Jiao, Carbon Monoxide Electroreduction as an Emerging Platform for Carbon Utilization, *Nat. Catal.*, 2019, **1**, 1062–1070, DOI: 10.1038/s41929-019-0388-2.

4 C. W. Li, J. Ciston and M. W. Kanan, Electroreduction of Carbon Monoxide to Liquid Fuel on Oxide-Derived Nanocrystalline Copper, *Nature*, 2014, **508**(7497), 504–507, DOI: 10.1038/nature13249.

5 X. Feng, K. Jiang, S. Fan and M. W. Kanan, A Direct Grain-Boundary-Activity Correlation for CO Electroreduction on Cu Nanoparticles, *ACS Cent. Sci.*, 2016, **2**(3), 169–174, DOI: 10.1021/ACSCENTSCI.6B00022/ASSET/IMAGES/LARGE/OC-2016-000225_0005.JPEG.

6 L. Wang, S. Nitopi, A. B. Wong, J. L. Snider, A. C. Nielander, C. G. Morales-Guio, M. Orazov, D. C. Higgins, C. Hahn and T. F. Jaramillo, Electrochemically Converting Carbon Monoxide to Liquid Fuels by Directing Selectivity with Electrode Surface Area, *Nat. Catal.*, 1929, **2**, 702–708, DOI: 10.1038/s41929-019-0301-z.

7 C. T. Dinh, F. P. García De Arquer, D. Sinton and E. H. Sargent, High Rate, Selective, and Stable Electroreduction of Co2 to Co in Basic and Neutral Media, *ACS Energy Lett.*, 2018, **3**(11), 2835–2840, DOI: 10.1021/ACSENERGYLETT.8B01734/SUPPL_FILE/NZ8B01734_SI_001.PDF.

8 J. H. Montoya, C. Shi, K. Chan and J. K. Nørskov, Theoretical Insights into a CO Dimerization Mechanism in CO2 Electroreduction, *J. Phys. Chem. Lett.*, 2015, **6**(11), 2032–2037, DOI: 10.1021/ACS.JPCLETT.5B00722/SUPPL_FILE/JZ5B00722_SI_001.PDF.

9 A. J. Garza, A. T. Bell and M. Head-Gordon, Mechanism of CO2 Reduction at Copper Surfaces: Pathways to C2 Products, *ACS Catal.*, 2018, **8**(2), 1490–1499, DOI: 10.1021/acscatal.7b03477.

10 S. Nitopi, E. Bertheussen, S. B. Scott, X. Liu, A. K. Engstfeld, S. Horch, B. Seger, I. E. L. Stephens, K. Chan, C. Hahn, J. K. Nørskov, T. F. Jaramillo and I. Chorkendorff, Progress and Perspectives of Electrochemical CO2 Reduction on Copper in Aqueous Electrolyte, *Chem. Rev.*, 2019, **119**(12), 7610–7672, DOI: 10.1021/acs.chemrev.8b00705.

11 R. Xia, J. J. Lv, X. Ma and F. Jiao, Enhanced Multi-Carbon Selectivity via CO Electroreduction Approach, *J. Catal.*, 2021, **398**, 185–191, DOI: 10.1016/J.JCAT.2021.03.034.

12 M. Jouny, W. Luc and F. Jiao, High-Rate Electroreduction of Carbon Monoxide to Multi-Carbon Products, *Nat. Catal.*, 2018, **1**(10), 748–755, DOI: 10.1038/s41929-018-0133-2.

13 X. Ding, J. Zhang and Y. Li, CO Electroreduction: What Can We Learn from Its Parent Reaction, CO2 Electroreduction?, *eScience*, 2023, 100137, DOI: 10.1016/J.ESCI.2023.100137.

2296 | *J. Mater. Chem. A*, 2025, **13**, 2285–2300

This journal is © The Royal Society of Chemistry 2025

14 G. L. De Gregorio, T. Burdyny, A. Loiudice, P. Iyengar, W. A. Smith and R. Buonsanti, Facet-Dependent Selectivity of Cu Catalysts in Electrochemical CO2 Reduction at Commercially Viable Current Densities, *ACS Catal.*, 2020, **10**(9), 4854–4862, DOI: **10.1021/ACSCATAL.0C00297/ASSET/ IMAGES/LARGE/CS0C00297_0004.JPEG**.

15 J. Liu, F. You, H. Bowen, Y. Wu, D. Wang, W. Zhou, C. Qian, G. Yang, G. Liu, H. Wang, Y. Guo, L. Gu, L. Feng, S. Li and Y. Zhao, Directing the Architecture of Surface-Clean Cu2O for CO Electroreduction, *J. Am. Chem. Soc.*, 2022, **144**(27), 12410–12420, DOI: **10.1021/JACS.2C04260**.

16 Y. Zhou, Y. Liang, J. Fu, K. Liu, Q. Chen, X. Wang, H. Li, L. Zhu, J. Hu, H. Pan, M. Miyauchi, L. Jiang, E. Cortés and M. Liu, Vertical Cu Nanoneedle Arrays Enhance the Local Electric Field Promoting C2 Hydrocarbons in the CO2 Electroreduction, *Nano Lett.*, 2022, **22**(5), 1963–1970, DOI: **10.1021/ACS.NANOLETT.1C04653/ASSET/IMAGES/LARGE/ NL1C04653_0004.JPEG**.

17 B.-B. Zhang, Y.-H. Wang, S.-M. Xu, K. Chen, Y.-G. Yang and Q.-H. Kong, Tuning Nanocavities of Au@Cu2O Yolk-Shell Nanoparticles for Highly Selective Electroreduction of CO2 to Ethanol at Low Potential, *RSC Adv.*, 2020, 19192–19198, DOI: **10.1039/d0ra02482a**.

18 D. Gao, Y. Zhang, Z. Zhou, F. Cai, X. Zhao, W. Huang, Y. Li, J. Zhu, P. Liu, F. Yang, G. Wang and X. Bao, Enhancing CO2 Electroreduction with the Metal–Oxide Interface, *J. Am. Chem. Soc.*, 2017, **139**, 5652–5655, DOI: **10.1021/ jacs.7b00102**.

19 N. Martić, C. Reller, C. Macauley, M. Löffler, A. M. Reichert, T. Reichbauer, K.-M. Vetter, B. Schmid, D. McLaughlin, P. Leidinger, D. Reinisch, C. Vogl, K. J. J. Mayrhofer, I. Katsounaros and G. Schmid, Ag2 Cu2O3 – a Catalyst Template Material for Selective Electroreduction of CO to C2+ Products, *Energy Environ. Sci.*, 2020, **13**(9), 2993–3006, DOI: **10.1039/d0ee01100b**.

20 Y. Hori, Electrochemical CO2 Reduction on Metal Electrodes, *Mod. Aspect. Electrochem.*, 2008, 89–189, DOI: **10.1007/978-0-387-49489-0_3**.

21 Y. Y. Birdja, E. Pérez-Gallent, M. C. Figueiredo, A. J. Göttle, F. Calle-Vallejo and M. T. M. Koper, Advances and Challenges in Understanding the Electrocatalytic Conversion of Carbon Dioxide to Fuels, *Nat. Energy*, 2019, 732–745, DOI: **10.1038/s41560-019-0450-y**.

22 R. Kortlever, J. Shen, K. J. P. Schouten, F. Calle-Vallejo and M. T. M. Koper, Catalysts and Reaction Pathways for the Electrochemical Reduction of Carbon Dioxide, *J. Phys. Chem. Lett.*, 2015, **6**(20), 4073–4082, DOI: **10.1021/ ACS.JPCLETT.5B01559/ASSET/IMAGES/LARGE/JZ-2015- 01559C_0004.JPEG**.

23 Y. Zheng, A. Vasileff, X. Zhou, Y. Jiao, M. Jaroniec and S. Z. Qiao, Understanding the Roadmap for Electrochemical Reduction of CO2 to Multi-Carbon Oxygenates and Hydrocarbons on Copper-Based Catalysts, *J. Am. Chem. Soc.*, 2019, **141**(19), 7646–7659, DOI: **10.1021/ JACS.9B02124**.

24 O. G. Sánchez, Y. Y. Birdja, M. Bulut, J. Vaes, T. Breugelmans and D. Pant, Recent Advances in Industrial CO2 Electroreduction, *Curr. Opin. Green Sustainable Chem.*, 2019, **16**, 47–56, DOI: **10.1016/J.COGSC.2019.01.005**.

25 W. Tang, A. A. Peterson, A. S. Varela, Z. P. Jovanov, L. Bech, W. J. Durand, S. Dahl, J. K. Nørskov and I. Chorkendorff, The Importance of Surface Morphology in Controlling the Selectivity of Polycrystalline Copper for CO2 Electroreduction, *Phys. Chem. Chem. Phys.*, 2011, **14**(1), 76–81, DOI: **10.1039/C1CP22700A**.

26 G. Zhang, Z. J. Zhao, D. Cheng, H. Li, J. Yu, Q. Wang, H. Gao, J. Guo, H. Wang, G. A. Ozin, T. Wang and J. Gong, Efficient CO2 Electroreduction on Facet-Selective Copper Films with High Conversion Rate, *Nat. Commun.*, 2021, **12**(1), 1–11, DOI: **10.1038/s41467-021-26053-w**.

27 P. Iyengar, M. J. Kolb, J. R. Pankhurst, F. Calle-Vallejo and R. Buonsanti, Elucidating the Facet-Dependent Selectivity for CO2 Electroreduction to Ethanol of Cu–Ag Tandem, *Catalysts*, 2021, **5**, 54, DOI: **10.1021/acscatal.1c00420**.

28 C. Chen, Y. Li, S. Yu, S. Louisia, J. Jin, M. Li, M. B. Ross and P. Yang, Cu-Ag Tandem Catalysts for High-Rate CO2 Electrolysis toward Multicarbons, *Joule*, 2020, **4**(8), 1688–1699, DOI: **10.1016/j.joule.2020.07.009**.

29 D. Niu, C. Wei, Z. Lu, Y. Fang, B. Liu, D. Sun, X. Hao, H. Pan and G. Wang, Cu2O-Ag Tandem Catalysts for Selective Electrochemical Reduction of CO2 to C2 Products, *Molecules*, 2021, **26**(8), 2175, DOI: **10.3390/ MOLECULES26082175**.

30 Y. Ma, J. Yu, M. Sun, B. Chen, X. Zhou, C. Ye, Z. Guan, W. Guo, G. Wang, S. Lu, D. Xia, Y. Wang, Z. He, L. Zheng, Q. Yun, L. Wang, J. Zhou, P. Lu, J. Yin, Y. Zhao, Z. Luo, L. Zhai, L. Liao, Z. Zhu, R. Ye, Y. Chen, Y. Lu, S. Xi, B. Huang, C.-S. Lee, Z. Fan, Y. Ma, J. Yu, B. Chen, X. Zhou, Z. Guan, W. Guo, S. Lu, Y. Wang, Z. He, Q. Yun, J. Zhou, P. Lu, J. Yin, Y. Zhao, Z. Luo, L. Zhai, L. Liao, Z. Zhu, R. Ye, C. S. Lee, Z. Fan, H. Kong Branch, M. Sun, B. Huang, G. Wang, L. Zheng, Y. Chen, D. Xia, L. Wang, Y. Lu and S. Xi, Confined Growth of Silver-Copper Janus Nanostructures with {100} Facets for Highly Selective Tandem Electrocatalytic Carbon Dioxide Reduction, *Adv. Mater.*, 2022, 2110607, DOI: **10.1002/ADMA.202110607**.

31 T. Zhang, J. C. Bui, J. C. Bui, Z. Li, A. T. Bell, A. Z. Weber and J. Wu, Highly Selective and Productive Reduction of Carbon Dioxide to Multicarbon Products via in Situ CO Management Using Segmented Tandem Electrodes, *Nat. Catal.*, 2022, **5**(3), 202–211, DOI: **10.1038/s41929-022-00751-0**.

32 E. L. Clark, C. Hahn, T. F. Jaramillo and A. T. Bell, Electrochemical CO 2 Reduction over Compressively Strained CuAg Surface Alloys with Enhanced Multi-Carbon Oxygenate Selectivity, *J. Am. Chem. Soc.*, 2017, **139**, 15848–15857, DOI: **10.1021/jacs.7b08607**.

33 T. T. H. Hoang, S. Verma, S. Ma, T. T. Fister, J. Timoshenko, A. I. Frenkel, P. J. A. Kenis and A. A. Gewirth, Nanoporous Copper-Silver Alloys by Additive-Controlled Electrodeposition for the Selective Electroreduction of CO2 to Ethylene and Ethanol, *J. Am. Chem. Soc.*, 2018, **140**(17), 5791–5797, DOI: **10.1021/jacs.8b01868**.

34 P. C. Chen, C. Chen, Y. Yang, A. L. Maulana, J. Jin, J. Feijoo and P. Yang, Chemical and Structural Evolution of AgCu

This journal is © The Royal Society of Chemistry 2025

*J. Mater. Chem. A*, 2025, **13**, 2285–2300 | **2297**

Catalysts in Electrochemical CO2 Reduction, *J. Am. Chem. Soc.*, 2023, **145**, 10116–10125, DOI: **10.1021/JACS.3C00467/ ASSET/IMAGES/LARGE/JA3C00467_0008.JPEG**.

35 Y. Zhong, X. Kong, Z. Song, Y. Liu, L. Peng, L. Zhang, X. Luo, J. Zeng and Z. Geng, Adjusting Local CO Confinement in Porous-Shell Ag@Cu Catalysts for Enhancing C-C Coupling toward CO2Eletroreduction, *Nano Lett.*, 2022, **22**(6), 2554– 2560, DOI: **10.1021/ACS.NANOLETT.1C04815/SUPPL_FILE/ NL1C04815_SI_001.PDF**.

36 L. R. L. Ting, P. Oriol, Y. Si Lim, M. Tanhaei, F. Calle-Vallejo and B. S. Yeo, Enhancing CO2 Electroreduction to Ethanol on Copper–Silver Composites by Opening an Alternative Catalytic Pathway, *ACS Catal.*, 2020, **10**, 4059–4069, DOI: **10.1021/acscatal.9b05319**.

37 J. Huang, M. Mensi, E. Oveisi, V. Mantella and R. Buonsanti, Structural Sensitivities in Bimetallic Catalysts for Electrochemical CO2 Reduction Revealed by Ag–Cu Nanodimers, *J. Am. Chem. Soc.*, 2019, 2490–2499, DOI: **10.1021/jacs.8b12381**.

38 X. Wang, Z. Wang, T. T. Zhuang, C. T. Dinh, J. Li, D. H. Nam, F. Li, C. W. Huang, C. S. Tan, Z. Chen, M. Chi, C. M. Gabardo, A. Seifitokaldani, P. Todorović, A. Proppe, Y. Pang, A. R. Kirmani, Y. Wang, A. H. Ip, L. J. Richter, B. Scheffel, A. Xu, S. C. Lo, S. O. Kelley, D. Sinton and E. H. Sargent, Efficient Upgrading of CO to C3 Fuel Using Asymmetric C-C Coupling Active Sites, *Nat. Commun.*, 2019, **10**(1), 1–7, DOI: **10.1038/s41467-019-13190-6**.

39 L. Wang, D. C. Higgins, Y. Ji, C. G. Morales-Guio, K. Chan, C. Hahn and T. F. Jaramillo, Selective Reduction of CO to Acetaldehyde with CuAg Electrocatalysts, *Proc. Natl. Acad. Sci. U. S. A.*, 2020, **117**(23), 12572–12575, DOI: **10.1073/ pnas.1821683117**.

40 A. Herzog, A. Bergmann, H. S. Jeon, J. Timoshenko, S. Kühl, C. Rettenmaier, M. Lopez Luna, F. T. Haase and B. Roldan Cuenya, Operando Investigation of Ag-Decorated Cu2O Nanocube Catalysts with Enhanced CO2 Electroreduction toward Liquid Products, *Angew. Chem. Int. Ed.*, 2021, **60**(13), 7426–7435, DOI: **10.1002/ANIE.202017070**.

41 C. G. Morales-Guio, E. R. Cave, S. A. Nitopi, J. T. Feaster, L. Wang, K. P. Kuhl, A. Jackson, N. C. Johnson, D. N. Abram, T. Hatsukade, C. Hahn and T. F. Jaramillo, Improved CO2 Reduction Activity towards C2+ Alcohols on a Tandem Gold on Copper Electrocatalyst, *Nat. Catal.*, 2018, **1**, 764–771, DOI: **10.1038/s41929-018-0139-9**.

42 Y. Qiao, G. Kastlunger, R. C. Davis, C. Andrés, G. Rodriguez, A. Vishart, W. Deng, Q. Xu, S. Li, P. Benedek, J. Chen, J. Schröder, J. Perryman, D. U. Lee, T. F. Jaramillo, I. Chorkendorff and B. Seger, Mechanistic Insights into Aldehyde Production from Electrochemical CO2 Reduction on CuAg Alloy via Operando X-Ray Measurements, *ACS Catal.*, 2023, 9379–9391, DOI: **10.1021/ACSCATAL.3C01009**.

43 J. Jiao, J. Wan, Y. Ma and Y. Wang, Facile Formation of Silver Nanoparticles as Plasmonic Photocatalysts for Hydrogen Production, *RSC Adv.*, 2016, **6**(107), 106031–106034, DOI: **10.1039/c6ra21269g**.

44 D. A. Svintsitskiy, T. Y. Kardash, O. A. Stonkus, E. M. Slavinskaya, A. I. Stadnichenko, S. V. Koscheev,

A. P. Chupakhin and A. I. Boronin, In Situ XRD, XPS, TEM, and TPR Study of Highly Active in Co Oxidation CuO Nanopowders, *J. Phys. Chem. C*, 2013, **117**(28), 14588– 14599, DOI: **10.1021/JP403339R/SUPPL_FILE/ JP403339R_SI_001.PDF**.

45 J. F. Xu, W. Ji, Z. X. Shen, S. H. Tang, X. R. Ye, D. Z. Jia and X. Q. Xin, Preparation and Characterization of CuO Nanocrystals, *J. Solid State Chem.*, 1999, **147**(2), 516–519, DOI: **10.1006/JSSC.1999.8409**.

46 L. S. Kibis, V. I. Avdeev, S. V. Koscheev and A. I. Boronin, Oxygen Species on the Silver Surface Oxidized by MW-Discharge: Study by Photoelectron Spectroscopy and DFT Model Calculations, *Surf. Sci.*, 2010, **604**(13–14), 1185– 1192, DOI: **10.1016/J.SUSC.2010.03.035**.

47 D. A. Svintsitskiy, T. Yu Kardash and A. I. Boronin, Surface Dynamics of Mixed Silver-Copper Oxide AgCuO2 during X-Ray Photoelectron Spectroscopy Study, *Appl. Surf. Sci.*, 2019, **463**, 300–309, DOI: **10.1016/J.APSUSC.2018.08.234**.

48 L. S. Kibis, A. I. Stadnichenko, E. M. Pajetnov, S. V. Koscheev, V. I. Zaykovskii and A. I. Boronin, The Investigation of Oxidized Silver Nanoparticles Prepared by Thermal Evaporation and Radio-Frequency Sputtering of Metallic Silver under Oxygen, *Appl. Surf. Sci.*, 2010, **257**(2), 404–413, DOI: **10.1016/J.APSUSC.2010.07.002**.

49 G. I. N. Waterhouse, G. A. Bowmaker and J. B. Metson, Oxidation of a Polycrystalline Silver Foil by Reaction with Ozone, *Appl. Surf. Sci.*, 2001, **183**(3–4), 191–204, DOI: **10.1016/S0169-4332(01)00561-X**.

50 S. Peters, S. Peredkov, M. Neeb, W. Eberhardt and M. Al-Hada, Size-Dependent XPS Spectra of Small Supported Au-Clusters, *Surf. Sci.*, 2013, **608**, 129–134, DOI: **10.1016/ J.SUSC.2012.09.024**.

51 M. C. Biesinger, Advanced Analysis of Copper X-Ray Photoelectron Spectra, *Surf. Interface Anal.*, 2017, **49**(13), 1325–1334, DOI: **10.1002/SIA.6239**.

52 L. Pauling, Atomic Radii and Interatomic Distances in Metals, *J. Am. Chem. Soc.*, 1947, **69**(3), 542–553, DOI: **10.1021/ja01195a024**.

53 Y. Liang, Z. Chen, W. Yao, P. Wang, S. Yu and X. Wang, Decorating of Ag and CuO on Cu Nanoparticles for Enhanced High Catalytic Activity to the Degradation of Organic Pollutants, *Langmuir*, 2017, **33**(31), 7606–7614, DOI: **10.1021/ACS.LANGMUIR.7B01540/ASSET/IMAGES/ LARGE/LA-2017-01540W_0008.JPEG**.

54 R. Yadav, D. P. Goyal, V. Kumar, P. Kumar, R. Meena, A. K. Mishra and A. Kandasami, Defect-Induced Phase Transformations in CuO Thin Films by Ag Ion Implantation and Their Gas-Sensing Applications, *J. Phys. Chem. C*, 2023, **127**(24), 11438–11447, DOI: **10.1021/ ACS.JPCC.3C01917/ASSET/IMAGES/LARGE/ JP3C01917_0009.JPEG**.

55 D. A. Svintsitskiy, T. Y. Kardash, O. A. Stonkus, E. M. Slavinskaya, A. I. Stadnichenko, S. V. Koscheev, A. P. Chupakhin and A. I. Boronin, In Situ XRD, XPS, TEM, and TPR Study of Highly Active in Co Oxidation CuO Nanopowders, *J. Phys. Chem. C*, 2013, **117**(28), 14588–

2298 | *J. Mater. Chem. A*, 2025, **13**, 2285–2300

This journal is © The Royal Society of Chemistry 2025

14599, DOI: **10.1021/JP403339R/SUPPL_FILE/JP403339R_SI_001.PDF**.

56 D. A. Svintsitskiy, T. Y. Kardash, E. M. Slavinskaya, O. A. Stonkus, S. V. Koscheev and A. I. Boronin, The Decomposition of Mixed Oxide Ag2Cu2O3: Structural Features and the Catalytic Properties in CO and C2H4 Oxidation, *Appl. Surf. Sci.*, 2018, **427**, 363–374, DOI: **10.1016/J.APSUSC.2017.08.010**.

57 G. Shi, J. Liu, B. Chen, Y. Bao and J. Xu, Phase-Controlled Growth of Cubic Phase CuO Nanoparticles by Chemical Vapor Deposition, *Phys. Status Solidi A*, 2017, **214**(10), 1700041, DOI: **10.1002/PSSA.201700041**.

58 O. S. Sitompul, X. Kong, X. Yu, Y. Zhao, J. L. Hernández-Ávila, J. de Urquijo, A. Gaur, B. D. Shrivastava and S. K. Joshi, Copper K-Edge XANES of Cu(I) and Cu(II) Oxide Mixtures, *J. Phys.:Conf. Ser.*, 2009, **190**(1), 012084, DOI: **10.1088/1742-6596/190/1/012084**.

59 EXAFS_Materials, *Reference X-Ray Spectra of Metal Foils*, Self Recorded, 2007, No. 925.

60 Y. Okamoto, T. Kubota, H. Gotoh, Y. Ohto, H. Aritani, T. Tanaka and S. Yoshida, XAFS Study of Zirconia-Supported Copper Catalysts for the NO–CO Reaction: Deactivation, Rejuvenation and Stabilization of Cu Species, *J. Chem. Soc., Faraday Trans.*, 1998, **94**(24), 3743–3752, DOI: **10.1039/A807152G**.

61 B. A. Manning, S. R. Kanel, E. Guzman, S. W. Brittle and I. E. Pavel, Oxidative Dissolution of Silver Nanoparticles by Synthetic Manganese Dioxide Investigated by Synchrotron X-Ray Absorption Spectroscopy, *J. Nanopart. Res.*, 2019, **21**(10), 1–14, DOI: **10.1007/S11051-019-4656-5/FIGURES/7**.

62 J. F. Moulder, W. F. Stickle, P. E. Sobol and K. D. Bomben, *Handbook of X-Ray Photoelectron Spectroscopy*, Edited By. Google Scholar, 1993.

63 S. V. Ganzha, S. N. Maksimova, S. N. Grushevskaya and A. V. Vvedenskii, Formation of Oxides on Copper in Alkaline Solution and Their Photoelectrochemical Properties, *Protect. Met. Phys. Chem. Surface*, 2011, **47**(2), 191–202, DOI: **10.1134/S2070205111020080/METRICS**.

64 Y. Zhao, X. Chang, A. S. Malkani, X. Yang, L. Thompson, F. Jiao and B. Xu, Speciation of Cu Surfaces during the Electrochemical CO Reduction Reaction, *J. Am. Chem. Soc.*, 2020, **142**(21), 9735–9743, DOI: **10.1021/JACS.0C02354/ASSET/IMAGES/LARGE/JA0C02354_0004.JPEG**.

65 M. Pellarin, I. Issa, C. Langlois, M. A. Lebeault, J. Ramade, J. Lermé, M. Broyer and E. Cottancin, Plasmon Spectroscopy and Chemical Structure of Small Bimetallic Cu(1-x)Agx Clusters, *J. Phys. Chem. C*, 2015, **119**(9), 5002–5012, DOI: **10.1021/JP511671M/SUPPL_FILE/JP511671M_SI_001.PDF**.

66 S. I. Bogatyrenko, A. P. Kryshtal and A. Kruk, Effect of Size on the Formation of Solid Solutions in Ag-Cu Nanoparticles, *J. Phys. Chem. C*, 2023, **127**(5), 2569–2580, DOI: **10.1021/ACS.JPCC.2C07132/ASSET/IMAGES/LARGE/JP2C07132_0013.JPEG**.

67 J. Vavra, T. H. Shen, D. Stoian, V. Tileli and R. Buonsanti, Real-Time Monitoring Reveals Dissolution/Redeposition Mechanism in Copper Nanocatalysts during the Initial Stages of the CO2 Reduction Reaction, *Angew. Chem., Int. Ed.*, 2021, **60**(3), 1347–1354, DOI: **10.1002/ANIE.202011137**.

68 J. Gao, J. Li, Y. Liu, M. Xia, Y. Z. Finfrock, S. M. Zakeeruddin, D. Ren and M. Grätzel, Solar Reduction of Carbon Dioxide on Copper-Tin Electrocatalysts with Energy Conversion Efficiency near 20%, *Nat. Commun.*, 2022, **13**(1), 1–11, DOI: **10.1038/s41467-022-33049-7**.

69 X. Wang, K. Klingan, M. Klingenhof, T. Möller, J. Ferreira de Araújo, I. Martens, A. Bagger, S. Jiang, J. Rossmeisl, H. Dau and P. Strasser, Morphology and Mechanism of Highly Selective Cu(II) Oxide Nanosheet Catalysts for Carbon Dioxide Electroreduction, *Nat. Commun.*, 2021, **12**(1), 1–12, DOI: **10.1038/s41467-021-20961-7**.

70 H. Yun, J. Kim, W. Choi, M. H. Han, J. H. Park, H. S. Oh, D. H. Won, K. Kwak and Y. J. Hwang, Understanding Morphological Degradation of Ag Nanoparticle during Electrochemical CO2 Reduction Reaction by Identical Location Observation, *Electrochim. Acta*, 2021, **371**, 137795, DOI: **10.1016/J.ELECTACTA.2021.137795**.

71 S. C. Lin, C. C. Chang, S. Y. Chiu, H. T. Pai, T. Y. Liao, C. S. Hsu, W. H. Chiang, M. K. Tsai and H. M. Chen, Operando Time-Resolved X-Ray Absorption Spectroscopy Reveals the Chemical Nature Enabling Highly Selective CO2 Reduction, *Nat. Commun.*, 2020, **11**(1), 1–12, DOI: **10.1038/s41467-020-17231-3**.

72 S. Zhang, S. Zhao, D. Qu, X. Liu, Y. Wu, Y. Chen, W. S. Huang Zhang, S. Zhao, D. Qu, X. Liu, Y. Wu, Y. Chen, S. Zhang and W. Huang, Electrochemical Reduction of CO2 Toward C2 Valuables on Cu@Ag Core-Shell Tandem Catalyst with Tunable Shell Thickness, *Small*, 2021, **17**(37), 2102293, DOI: **10.1002/SMLL.202102293**.

73 R. Betancourt-Galindo, P. Y. Reyes-Rodriguez, B. A. Puente-Urbina, C. A. Avila-Orta, O. S. Rodríguez-Fernández, G. Cadenas-Pliego, R. H. Lira-Saldivar and L. A. García-Cerda, Synthesis of Copper Nanoparticles by Thermal Decomposition and Their Antimicrobial Properties, *J. Nanomater.*, 2014, **2014**, 980545, DOI: **10.1155/2014/980545**.

74 Y. Yu, D. Wang, Y. Hong, T. Zhang, C. Liu, J. Chen, G. Qin and S. Li, Bulk-Immiscible CuAg Alloy Nanorods Prepared by Phase Transition from Oxides for Electrochemical CO2 Reduction, *Chem. Commun.*, 2022, **58**(79), 11163–11166, DOI: **10.1039/D2CC04789F**.

75 C. Yang, B. H. Ko, S. Hwang, Z. Liu, Y. Yao, W. Luc, M. Cui, A. S. Malkani, T. Li, X. Wang, J. Dai, B. Xu, G. Wang, D. Su, F. Jiao and L. Hu, Overcoming Immiscibility toward Bimetallic Catalyst Library, *Sci. Adv.*, 2020, **6**(17), eaaz6844, DOI: **10.1126/SCIADV.AAZ6844/SUPPL_FILE/AAZ6844_SM.PDF**.

76 J. Wang, X. Liu, R. Li, Z. Li, X. Wang, H. Wang, Y. Wu, S. Jiang and Z. Lu, Formation Mechanism and Characterization of Immiscible Nanoporous Binary Cu–Ag Alloys with Excellent Surface-Enhanced Raman Scattering Performance by Chemical Dealloying of Glassy Precursors, *Inorg. Chem. Front.*, 2020, **7**(5), 1127–1139, DOI: **10.1039/C9QI01521C**.

77 E. Pérez-Gallent, G. Marcandalli, M. C. Figueiredo, F. Calle-Vallejo and M. T. M. Koper, Structure- and Potential-Dependent Cation Effects on CO Reduction at Copper

This journal is © The Royal Society of Chemistry 2025

*J. Mater. Chem. A*, 2025, **13**, 2285–2300 | **2299**

Single-Crystal Electrodes, *J. Am. Chem. Soc.*, 2017, **139**(45), 16412–16419, DOI: **10.1021/jacs.7b10142**.

78  S. Strehle, S. Menzel, H. Wendrock, J. Acker and K. Wetzig, Microstructural Investigation of Electrodeposited CuAg-Thin Films, *Microelectron. Eng.*, 2003, **70**(2–4), 506–511, DOI: **10.1016/S0167-9317(03)00422-2**.

79  C. C. Jian, J. Zhang and X. Ma, Cu–Ag Alloy for Engineering Properties and Applications Based on the LSPR of Metal Nanoparticles, *RSC Adv.*, 2020, **10**(22), 13277–13285, DOI: **10.1039/D0RA01474E**.

80  S. Lee, G. Park and J. Lee, Importance of Ag-Cu Biphasic Boundaries for Selective Electrochemical Reduction of CO2 to Ethanol, *ACS Catal.*, 2017, **7**(12), 8594–8604, DOI: **10.1021/ACSCATAL.7B02822/ASSET/IMAGES/LARGE/CS-2017-028225_0010.JPEG**.

81  D. Bokov, A. Turki Jalil, S. Chupradit, W. Suksatan, M. Javed Ansari, I. H. Shewael, G. H. Valiev and E. Kianfar, Nanomaterial by Sol-Gel Method: Synthesis and Application, *Adv. Mater. Sci. Eng.*, 2021, **2021**, 102014, DOI: **10.1155/2021/5102014**.

82  A. Vasileff, C. Xu, Y. Jiao, Y. Zheng and S. Z. Qiao, Surface and Interface Engineering in Copper-Based Bimetallic Materials for Selective CO2 Electroreduction, *Chem*, 2018, **4**(8), 1809–1831, DOI: **10.1016/J.CHEMPR.2018.05.001**.

83  S. Yang, W. Kim and M. Cho, Molecular Dynamics Study on the Coalescence Kinetics and Mechanical Behavior of Nanoporous Structure Formed by Thermal Sintering of Cu Nanoparticles, *Int. J. Eng. Sci.*, 2018, **123**, 1–19, DOI: **10.1016/J.IJENGSCI.2017.11.008**.

**2300** | *J. Mater. Chem. A*, 2025, **13**, 2285–2300

This journal is © The Royal Society of Chemistry 2025